Brian P. Mann[1]
Department of Mechanical and Aerospace Engineering,
University of Missouri,
Columbia, MO 65203
e-mail: mannbr@missouri.edu

Keith A. Young
Advanced Manufacturing R&D,
The Boeing Company,
St. Louis, MO 62166

Tony L. Schmitz
Department of Mechanical and Aerospace Engineering,
University of Florida,
Gainesville, FL 32611

David N. Dilley
D3 Vibrations, Inc.,
220 S. Main Street,
Royal Oak, MI 48067

Simultaneous Stability and Surface Location Error Predictions in Milling

Optimizing the milling process requires a priori knowledge of many process variables. However, the ability to include both milling stability and accuracy information is limited because current methods do not provide simultaneous milling stability and accuracy predictions. The method described within this paper, called Temporal Finite Element Analysis (TFEA), provides an approach for simultaneous prediction of milling stability and surface location error. This paper details the application of this approach to a multiple mode system in two orthogonal directions. The TFEA method forms an approximate analytical solution by dividing the time in the cut into a finite number of elements. The approximate solution is then matched with the exact solution for free vibration to obtain a discrete linear map. The formulated dynamic map is then used to determine stability, steady-state surface location error, and to reconstruct the time series for a stable cutting process. Solution convergence is evaluated by simply increasing the number of elements and through comparisons with numerical integration. Analytical predictions are compared to several different milling experiments. An interesting period two behavior, which was originally believed to be a flip bifurcation, was observed during experiment. However, evidence is presented to show this behavior can be attributed to runout in the cutter teeth. [DOI: 10.1115/1.1948394]

1 Introduction

Increased industrial competition has driven the need for manufacturers to reduce costs and increase dimensional accuracy. The optimization of manufacturing processes offers businesses substantial financial benefits and an opportunity to gain a competitive edge. Predictive machining models can be applied to improve process efficiencies, dimensional accuracy, and part quality. Dynamic models provide the ability to predict surface accuracy and regions of stable cutting for a large combination of process parameters. This allows businesses to use analysis and/or simulation for process optimization rather than costly trial and error.

Relative vibrations between a cutting tool and workpiece can result in a machining process with surface location errors and time-varying chip loads. Since cutting forces are approximately proportional to the uncut chip area [1–4], chip load variations cause dynamic cutting forces which may excite the structural modes of a machine-tool system resulting in unstable vibrations known as *chatter*. Unless avoided, chatter vibrations may cause large dynamic loads on the machine spindle and table structure, damage to the cutting tool, and a poor surface finish [1,5]. Therefore, it is desirable to avoid chatter vibrations. Even in the absence of chatter, the accurate placement of a machined surface can be complicated by dynamic motions which cause the machined surface not to lie exactly at the commanded location [6].

The research of Tlusty, Tobias, and Merrit provided mathematical process models to explain chatter, including the development of stability lobe diagrams that are used to compactly represent stability information as a function of spindle speed and depth of cut [7–9]. A number of related efforts are listed in Refs. [7–27], which also include studies of nonlinear system behavior. The equations describing the machining dynamics are in the form of delay-differential equations, where the delay represents the time between tool passages.

Stability predictions from earlier analyses are only approximate for the case of milling, since they rely on the fundamental assumption of continuous cutting. In milling, the cutting forces change direction with tool rotation and cutting is interrupted as each tooth enters and leaves the workpiece. This leads to cutting force coefficients which change from zero (when the tool is free) to large numbers (when the tool is cutting). While numerical simulation can be used to capture the interrupted nature of the milling process [1,19,28], the exploration of parameter space by time domain simulation is clearly inefficient. The focus of many recent investigations has been the occurrence of new bifurcation phenomena in interrupted cutting processes. In addition to Hopf bifurcations, period-doubling bifurcations have been analytically predicted in Refs. [3,29–31] and confirmed experimentally in Refs. [3,31–33].

In this paper, an approach for simultaneous predictions of milling stability and surface location error is generalized to account for multiple modes along two orthogonal directions. The solution technique, called Temporal Finite Element Analysis or (TFEA), forms an approximate solution by dividing the time in the cut into a finite number of elements. To solve the interrupted cutting problem, the approximate solution during cutting is matched with the exact solution for free vibration to obtain a discrete linear map. Eigenvalues of the map are used to determine stability; fixed points of the map are used for predicting the steady-state surface location error and time series reconstruction. The analysis presented here avoids the need for time marching or iteration to determine the important dynamic behavior of the milling process.

Results from three different experimental cutting tests are compared to analytical predictions. Stability predictions for a flexible tool and rigid workpiece are compared to a milling system with two degrees of freedom. Surface location error predictions are compared for the following experiments: (1) a flexible workpiece and rigid tool; and (2) a rigid workpiece and flexible tool. In all cases, the results from experimental cutting tests show strong agreement with theoretical predictions.

[1]To whom correspondence should be addressed.

Contributed by the Manufacturing Engineering Division for publication in the ASME JOURNAL OF MANUFACTURING SCIENCE AND ENGINEERING. Manuscript received January 16, 2004; final revision received July 8, 2004. Associate Editor: D.-W. Cho.

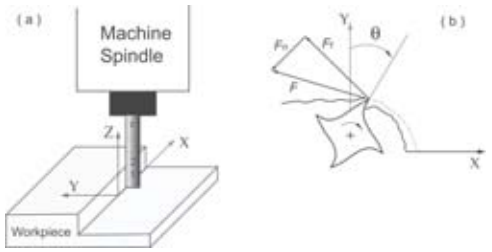

Fig. 1 Multiple degree of freedom schematic of the milling process: (a) Spatial representation of machine tool structure at discrete locations along the tool; and (b) Up-milling schematic diagram of tool tip in-plane motion

2 Model Development

2.1 Modal Equations of Motion. In this section we seek to generalize the TFEA method by analyzing a typical machine tool structure with $2\times r$ degrees of freedom (see Fig. 1). The displacement at discrete points along the structure is defined by vectors $\boldsymbol{x}(t)=[x_1(t)x_2(t)\cdots x_r(t)]^{\mathsf{T}}$ and $\boldsymbol{y}(t)=[y_1(t)y_2(t)\cdots y_r(t)]^{\mathsf{T}}$. A summation of forces produces the following equation of motion:

$$\begin{bmatrix}\mathbf{M}_{xx} & \mathbf{M}_{xy}\\ \mathbf{M}_{yx} & \mathbf{M}_{yy}\end{bmatrix}\begin{bmatrix}\ddot{\boldsymbol{x}}(t)\\ \ddot{\boldsymbol{y}}(t)\end{bmatrix}+\begin{bmatrix}\mathbf{C}_{xx} & \mathbf{C}_{xy}\\ \mathbf{C}_{yx} & \mathbf{C}_{yy}\end{bmatrix}\begin{bmatrix}\dot{\boldsymbol{x}}(t)\\ \dot{\boldsymbol{y}}(t)\end{bmatrix}+\begin{bmatrix}\mathbf{K}_{xx} & \mathbf{K}_{xy}\\ \mathbf{K}_{yx} & \mathbf{K}_{yy}\end{bmatrix}\begin{bmatrix}\boldsymbol{x}(t)\\ \boldsymbol{y}(t)\end{bmatrix}=\begin{bmatrix}\boldsymbol{F}_x(t)\\ \boldsymbol{F}_y(t)\end{bmatrix}, \tag{1}$$

where the cutting force vectors are written as $\boldsymbol{F}_{x,y}$ and the terms $\mathbf{M}_{x,y}$, $\mathbf{C}_{x,y}$, and $\mathbf{K}_{x,y}$ represent the discrete system mass, damping, and stiffness matrices. The spatial equation of motion can be written as a modal matrix equation using the following linear coordinate transformation:

$$\boldsymbol{x}(t)=\mathbf{U}_x\boldsymbol{q}_x(t),\quad \boldsymbol{y}(t)=\mathbf{U}_y\boldsymbol{q}_y(t), \tag{2}$$

where $\mathbf{U}_x$ and $\mathbf{U}_y$ are the structural mode shapes in the x- and y-directions, respectively, which relate the spatial displacements along the structure to the modal displacement vectors $\boldsymbol{q}_x(t)$ and $\boldsymbol{q}_y(t)$. Assuming uncoupled motions in the x- and y-directions ($\mathbf{M}_{xy}=\mathbf{M}_{yx}=\mathbf{C}_{xy}=\mathbf{C}_{yx}=\mathbf{K}_{xy}=\mathbf{K}_{yx}=0$), the modal matrix equation of motion becomes

$$\begin{bmatrix}\mathbf{U}_x^{\mathsf{T}}\mathbf{M}_{xx}\mathbf{U}_x & 0\\ 0 & \mathbf{U}_y^{\mathsf{T}}\mathbf{M}_{yy}U_y\end{bmatrix}\begin{bmatrix}\ddot{\boldsymbol{q}}_x(t)\\ \ddot{\boldsymbol{q}}_y(t)\end{bmatrix}+\begin{bmatrix}\mathbf{U}_x^{\mathsf{T}}\mathbf{C}_{xx}\mathbf{U}_x & 0\\ 0 & \mathbf{U}_y^{\mathsf{T}}\mathbf{C}_{yy}\mathbf{U}_y\end{bmatrix}\times\begin{bmatrix}\dot{\boldsymbol{q}}_x(t)\\ \dot{\boldsymbol{q}}_y(t)\end{bmatrix}+\begin{bmatrix}\mathbf{U}_x^{\mathsf{T}}\mathbf{K}_{xx}\mathbf{U}_x & 0\\ 0 & \mathbf{U}_y^{\mathsf{T}}\mathbf{K}_{yy}\mathbf{U}_y\end{bmatrix}\begin{bmatrix}\boldsymbol{q}_x(t)\\ \boldsymbol{q}_y(t)\end{bmatrix}=\begin{bmatrix}\mathbf{U}_x^{\mathsf{T}}\boldsymbol{F}_x(t)\\ \mathbf{U}_y^{\mathsf{T}}\boldsymbol{F}_y(t)\end{bmatrix}. \tag{3}$$

Equation (3) can be written more compactly as

$$\mathbf{M}_q\ddot{\boldsymbol{q}}(t)+\mathbf{C}_q\dot{\boldsymbol{q}}(t)+\mathbf{K}_q\boldsymbol{q}(t)=\begin{bmatrix}\mathbf{U}_x^{\mathsf{T}}\boldsymbol{F}_x(t)\\ \mathbf{U}_y^{\mathsf{T}}\boldsymbol{F}_y(t)\end{bmatrix}, \tag{4}$$

where $\boldsymbol{q}(t)=[\boldsymbol{q}_x(t)^{\mathsf{T}}\boldsymbol{q}_y(t)^{\mathsf{T}}]^{\mathsf{T}}$ is the $2r\times 1$ modal displacement vector. For the peripheral end milling operations under consideration, the cutting forces $F_{x1}(t)$ and $F_{y1}(t)$ can be assumed to act only at the tool tip,

$$\boldsymbol{F}_x(t)=[F_{x1}(t)0\cdots 0]^{\mathsf{T}},\quad \boldsymbol{F}_y(t)=[F_{y1}(t)0\cdots 0]^{\mathsf{T}}. \tag{5}$$

Assuming the structural modes have been unit normalized at the tool tip, the right-hand side of Eq. (4) becomes

$$\boldsymbol{F}_q(t)=\begin{bmatrix}\mathbf{U}_x^{\mathsf{T}}\boldsymbol{F}_x(t)\\ \mathbf{U}_y^{\mathsf{T}}\boldsymbol{F}_y(t)\end{bmatrix}_{2r\times 1}=[F_{x1}(t)\cdots F_{x1}(t)F_{y1}(t)\cdots F_{y1}(t)]^{\mathsf{T}}, \tag{6}$$

and the modal equation of motion becomes

$$\mathbf{M}_q\ddot{\boldsymbol{q}}(t)+\mathbf{C}_q\dot{\boldsymbol{q}}(t)+\mathbf{K}_q\boldsymbol{q}(t)=\boldsymbol{F}_q(t). \tag{7}$$

The formulation of Eq. (7) is significant in the sense that system identification need only be performed at the tool tip to obtain an adequate system model.

2.2 Cutting Force Model. The total cutting force in each direction can be written as a summation over the total number of cutting teeth N,

$$F_{x1}(t)=-\sum_{p=1}^{N}g_p(t)[F_{tp}(t)\cos\theta_p(t)+F_{np}(t)\sin\theta_p(t)], \tag{8}$$

$$F_{y1}(t)=\sum_{p=1}^{N}g_p(t)[F_{tp}(t)\sin\theta_p(t)-F_{np}(t)\cos\theta_p(t)], \tag{9}$$

where $g_p(t)$ acts as a switching function, it is equal to one if the pth tooth is active and zero if it is not cutting [18,20]. The tangential and normal cutting force components, $F_{tp}(t)$ and $F_{np}(t)$ respectively, are considered to be a function of cutting pressures K_t and K_n, edge coefficients K_{te} and K_{ne} [5], the axial depth of cut b, and the instantaneous chip thickness $w_p(t)$,

$$F_{tp}(t)=K_tbw_p(t)+K_{te}b, \tag{10}$$

$$F_{np}(t)=K_nbw_p(t)+K_{ne}b, \tag{11}$$

where $w_p(t)$ depends upon the feed per tooth, h, the cutter rotation angle $\theta_p(t)$, and regeneration in the compliant tool directions:

$$w_p(t)=h\sin\theta_p(t)+[x_1(t)-x_1(t-\tau)]\sin\theta_p(t)+[y_1(t)-y_1(t-\tau)]\cos\theta_p(t). \tag{12}$$

Here $\tau=60/N\Omega(\mathrm{s})$ is the tooth passing period, Ω is the spindle speed given in (rpm), and N is the total number of cutting teeth.

Substitution of Eqs. (10)–(12) into Eqs. (8) and (9) gives an expanded expression for the cutting forces,

$$\begin{bmatrix}F_{x1}(t)\\ F_{y1}(t)\end{bmatrix}=\sum_{p=1}^{N}g_p(t)b\left(h\begin{bmatrix}-K_tsc-K_ns^2\\ K_ts^2-K_nsc\end{bmatrix}+\begin{bmatrix}-K_{te}c-K_{ne}s\\ K_{te}s-K_{ne}c\end{bmatrix}+\begin{bmatrix}-K_tsc-K_ns^2 & -K_tc^2-K_nsc\\ K_ts^2-K_nsc & K_tsc-K_nc^2\end{bmatrix}\times\begin{bmatrix}x_1(t)-x_1(t-\tau)\\ y_1(t)-y_1(t-\tau)\end{bmatrix}\right), \tag{13}$$

where $s=\sin\theta_p(t)$ and $c=\cos\theta_p(t)$. Equation (13) can be written more compactly by defining

$$\mathbf{K}_c^*(t)=\sum_{p=1}^{N}g_p(t)\begin{bmatrix}-K_tsc-K_ns^2 & -K_tc^2-K_nsc\\ K_ts^2-K_nsc & K_tsc-K_nc^2\end{bmatrix}, \tag{14}$$

$$\boldsymbol{f}_o^*(t)=\sum_{p=1}^{N}g_p(t)\left(h\begin{bmatrix}-K_tsc-K_ns^2\\ K_ts^2-K_nsc\end{bmatrix}+\begin{bmatrix}-K_{te}c-K_{ne}s\\ K_{te}s-K_{ne}c\end{bmatrix}\right). \tag{15}$$

Substituting these terms along with the normalized modes shapes from Eq. (2) into Eq. (13) gives the cutting force in terms of the modal displacements:

$$\begin{bmatrix}F_{x1}(t)\\ F_{y1}(t)\end{bmatrix}=b\mathbf{K}_c^*(t)\begin{bmatrix}1\ldots 1,0\ldots 0\\ 0\ldots 0,1\ldots 1\end{bmatrix}\begin{bmatrix}\boldsymbol{q}_x(t)-\boldsymbol{q}_x(t-\tau)\\ \boldsymbol{q}_y(t)-\boldsymbol{q}_y(t-\tau)\end{bmatrix}+b\boldsymbol{f}_o^*(t), \tag{16}$$

Inserting Eq. (16) into Eq. (6) and reassembling the modal matrix equation of motion gives

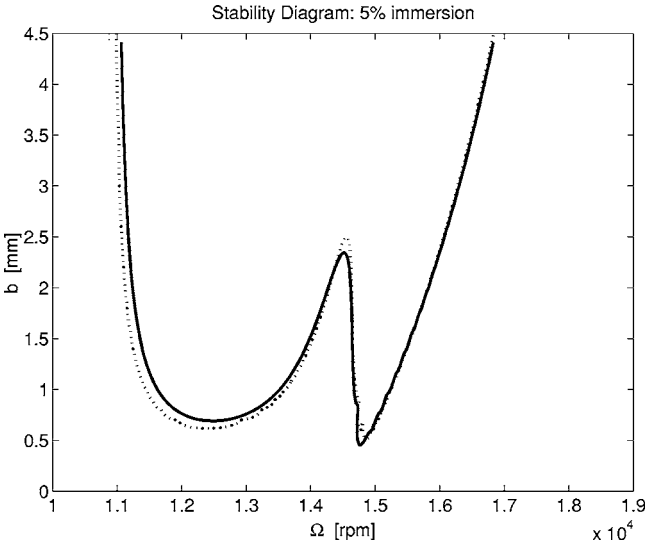

Fig. 2 Comparison of predicted stability boundaries with Euler Integration (dotted line) and TFEA (solid line). Aluminum cutting coeficients, listed in Section 4, were applied along with the modal parameters for the 12.75 (mm) tool, listed in Table 1, to create this diagram.

$$\mathbf{M}_q\ddot{\boldsymbol{q}}(t)+\mathbf{C}_q\dot{\boldsymbol{q}}(t)+\mathbf{K}_q\boldsymbol{q}(t)=b\mathbf{K}_c(t)[\boldsymbol{q}(t)-\boldsymbol{q}(t-\tau)]+b\boldsymbol{f}_o(t), \tag{17}$$

where $\mathbf{K}_c(t)$ is a $2r\times 2r$ matrix and $\boldsymbol{f}_o(t)$ is a $2r\times 1$ vector.

3 Analysis Approach

The dynamic behavior of the milling process is described by a time-delay differential equation which does not have a closed form solution. Therefore, an approximate solution is sought to understand the behavior of the system. The analysis approach shown in this section formulates a discrete linear map by matching an approximate solution for the cutting motion, obtained by dividing the time in the cut into a finite number of elements, to the exact solution for free vibration. As shown in previous Refs. [31–36], a convergence to the exact solution is obtained by simply increasing the number of elements during the cutting time.

The formulated dynamic map is then used in three different ways: (1) stability prediction from the magnitude of map characteristic multipliers; (2) prediction of steady-state surface location error from map fixed points; and (3) reconstruction of the stable cutting motion time series. The analysis presented in this article extends the previous stability and surface location error work from Refs. [32,33,36] to account for the contribution of multiple modes in two orthogonal directions.

3.1 Free Vibration. When the tool is not in contact with the workpiece, the system is governed by the equation for free vibration,

$$\mathbf{M}_q\ddot{\boldsymbol{q}}(t)+\mathbf{C}_q\dot{\boldsymbol{q}}(t)+\mathbf{K}_q\boldsymbol{q}(t)=0. \tag{18}$$

This equation can be rearranged into state-space form,

$$\begin{bmatrix}\dot{\boldsymbol{q}}(t)\\ \ddot{\boldsymbol{q}}(t)\end{bmatrix}=\begin{bmatrix}0 & \mathbf{I}\\ -\mathbf{M}_q^{-1}\mathbf{K}_q & -\mathbf{M}_q^{-1}\mathbf{C}_q\end{bmatrix}\begin{bmatrix}\boldsymbol{q}(t)\\ \dot{\boldsymbol{q}}(t)\end{bmatrix} \tag{19}$$

where the $4r\times 4r$ state matrix in Eq. (19) will be denoted by $\mathbf{G}$. If we let t_c be the time the tool leaves the material and t_f be the duration of free vibration, a state transition matrix ($\mathbf{\Phi}=e^{\mathbf{G}t_f}$) can be obtained that relates the state of the tool at the beginning of free vibration to the state of the tool at the end of free vibration.

This equation is true for every period, such that for all n:

$$\begin{bmatrix}\boldsymbol{q}(n\tau)\\ \dot{\boldsymbol{q}}(n\tau)\end{bmatrix}=\mathbf{\Phi}\begin{bmatrix}\boldsymbol{q}((n-1)\tau+t_c)\\ \dot{\boldsymbol{q}}((n-1)\tau+t_c)\end{bmatrix}. \tag{20}$$

3.2 Vibration During Cutting. When the tool is in the cut, its motion is governed by a time-delayed differential equation. Since this equation does not have a closed form solution, an approximate solution for the modal displacement of the tool is assumed for the jth element of the nth tooth passage as a linear combination of polynomials (see Peters et al. [37]):

$$\boldsymbol{q}(t)=\sum_{i=1}^{4}\boldsymbol{a}_{ji}^{n}\phi_i(\sigma_j(t)). \tag{21}$$

Here, $\sigma_j(t)=t-n\tau-\Sigma_{k=1}^{j-1}t_k$ is the "local" time within the jth element of the nth period, the length of the kth element is t_k, and the trial functions $\phi_i(\sigma_j(t))$ are cubic Hermite polynomials [35].

Substitution of the assumed solution [Eq. (21)] into the equation of motion [Eq. (17)] leads to a nonzero error. The error from the assumed solution is "weighted" by multiplying by a set of test functions and setting the integral of the weighted error to zero to obtain two equations per element [31,34,37–39]. The test functions are chosen to be: $\psi_1(\sigma_j)=1$ (constant) and $\psi_2(\sigma_j)=\sigma_j/t_j-1/2$ (linear). The integral is taken over the time for each element, $t_j=t_c/E$, thereby dividing the time in the cut t_c into E elements. The resulting two equations are

$$\int_0^{t_j}\left[\mathbf{M}_q\left(\sum_{i=1}^{4}\boldsymbol{a}_{ji}^{n}\ddot{\phi}_i(\sigma_j)\psi_p(\sigma_j)\right)+\mathbf{C}_q\left(\sum_{i=1}^{4}\boldsymbol{a}_{ji}^{n}\dot{\phi}_i(\sigma_j)\psi_p(\sigma_j)\right)+(\mathbf{K}_q-b\mathbf{K}_c(\sigma_j))\left(\sum_{i=1}^{4}\boldsymbol{a}_{ji}^{n}\phi_i(\sigma_j)\psi_p(\sigma_j)\right)+b\mathbf{K}_c(\sigma_j)\times\left(\sum_{i=1}^{4}\boldsymbol{a}_{ji}^{n-1}\phi_i(\sigma_j)\psi_p(\sigma_j)\right)-b\boldsymbol{f}_o(\sigma_j)\psi_p(\sigma_j)\right]d\sigma_j=0,\quad p=1,2, \tag{22}$$

where $\mathbf{K}_c(\sigma_j)$ and $\boldsymbol{f}_o(\sigma_j)$ have been used in place of the previously defined $\mathbf{K}_c(t)$ and $\boldsymbol{f}_o(t)$ to explicitly show their dependence on the local time.

The modal displacement and modal velocity at tool entry into the cut are specified by the coefficients of the first two basis functions on the first element: $\boldsymbol{a}_{11}^{n}$ and $\boldsymbol{a}_{12}^{n}$. The relationship between the initial and final conditions during free vibration can be rewritten in terms of the coefficients as

$$\begin{pmatrix}\boldsymbol{a}_{11}\\ \boldsymbol{a}_{12}\end{pmatrix}^{n}=\mathbf{\Phi}\begin{pmatrix}\boldsymbol{a}_{E3}\\ \boldsymbol{a}_{E4}\end{pmatrix}^{n-1}, \tag{23}$$

where E is the total number of elements in the cut. For the remainder of the elements, a continuity constraint is imposed to set the position and velocity at the end of one element equal to the position and velocity at the beginning of the next element.

Equations (22) and (23) can be arranged into a global matrix relating the coefficients in the current tooth passage to the coefficients in the previous tooth passage. The following expression is for the case when the number of elements is $E=3$:

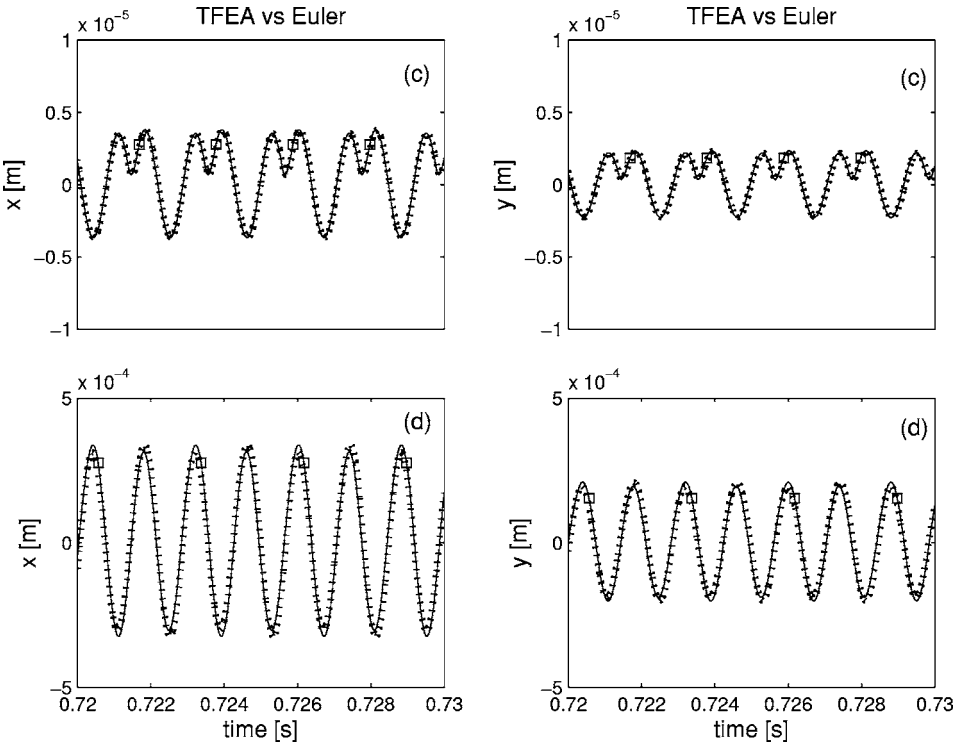

Fig. 3 A comparison of steady-state displacement predictions between Euler Integration (solid line) and TFEA (dotted line). Each row contains the *x*- and *y*-tool displacements, with a 1/tooth mark shown by a □, for the following cutting parameters: (c) corresponds to [Ω =14300 (rpm), *b*=0.3 (mm)]; and (d) corresponds to [Ω=10,700 (rpm), *b*=3.0 (mm)]. Aluminum cutting coefficients, listed in Sec. 4, were applied along with the modal parameters for the 12.75 (mm) tool, listed in Table 1, to create this diagram.

$$\begin{bmatrix} \mathbf{I} & \mathbf{0} & \mathbf{0} & \mathbf{0} \\ \mathbf{N}_1^1 & \mathbf{N}_2^1 & \mathbf{0} & \mathbf{0} \\ \mathbf{0} & \mathbf{N}_1^2 & \mathbf{N}_2^2 & \mathbf{0} \\ \mathbf{0} & \mathbf{0} & \mathbf{N}_1^3 & \mathbf{N}_2^3 \end{bmatrix} \begin{bmatrix} \boldsymbol{a}_{11} \\ \boldsymbol{a}_{12} \\ \boldsymbol{a}_{21} \\ \boldsymbol{a}_{22} \\ \boldsymbol{a}_{31} \\ \boldsymbol{a}_{32} \\ \boldsymbol{a}_{33} \\ \boldsymbol{a}_{34} \end{bmatrix}^n = \begin{bmatrix} \mathbf{0} & \mathbf{0} & \mathbf{0} & \mathbf{\Phi} \\ \mathbf{P}_1^1 & \mathbf{P}_2^1 & \mathbf{0} & \mathbf{0} \\ \mathbf{0} & \mathbf{P}_1^2 & \mathbf{P}_2^2 & \mathbf{0} \\ \mathbf{0} & \mathbf{0} & \mathbf{P}_1^3 & \mathbf{P}_2^3 \end{bmatrix} \begin{bmatrix} \boldsymbol{a}_{11} \\ \boldsymbol{a}_{12} \\ \boldsymbol{a}_{21} \\ \boldsymbol{a}_{22} \\ \boldsymbol{a}_{31} \\ \boldsymbol{a}_{32} \\ \boldsymbol{a}_{33} \\ \boldsymbol{a}_{34} \end{bmatrix}^{n-1} + \begin{bmatrix} \mathbf{0} \\ \mathbf{0} \\ \boldsymbol{C}_1^1 \\ \boldsymbol{C}_2^1 \\ \boldsymbol{C}_1^2 \\ \boldsymbol{C}_2^2 \\ \boldsymbol{C}_1^3 \\ \boldsymbol{C}_2^3 \end{bmatrix}, \tag{24}$$

where the submatrices and elements of the submatrices for the *j*th element are

$$\mathbf{N}_1^j = \begin{bmatrix} N_{11}^j & N_{12}^j \\ N_{21}^j & N_{22}^j \end{bmatrix}, \quad \mathbf{N}_2^j = \begin{bmatrix} N_{13}^j & N_{14}^j \\ N_{23}^j & N_{24}^j \end{bmatrix}, \tag{25}$$

$$\mathbf{P}_1^j = \begin{bmatrix} P_{11}^j & P_{12}^j \\ P_{21}^j & P_{22}^j \end{bmatrix}, \quad \mathbf{P}_2^j = \begin{bmatrix} P_{13}^j & P_{14}^j \\ P_{23}^j & P_{24}^j \end{bmatrix}, \tag{26}$$

$$N_{pi}^j = \int_0^{t_j} [\mathbf{M}_q \ddot{\phi}_i(\sigma_j) + \mathbf{C}_q \dot{\phi}_i(\sigma_j) + (\mathbf{K}_q - b\mathbf{K}_c(\sigma_j))\phi_i(\sigma_j)]\psi_p(\sigma_j) d\sigma_j, \tag{27}$$

$$P_{pi}^j = \int_0^{t_j} -b\mathbf{K}_c(\sigma_j)\phi_i(\sigma_j)\psi_p(\sigma_j) d\sigma_j, \tag{28}$$

$$C_p^j = \int_0^{t_j} b\boldsymbol{f}_o(\sigma_j)\psi_p d\sigma_j. \tag{29}$$

The dimensions for the global matrix equations are $(4r+4rE \times 4r+4rE)$, which illustrates the size of the matrices will quickly increase as the number of structural modes (r) becomes larger.

Equation (24) describes a discrete dynamical system, or map, that can be written as

$$\mathbf{A}\boldsymbol{a}_n = \mathbf{B}\boldsymbol{a}_{n-1} + \boldsymbol{C}, \tag{30}$$

or

$$\boldsymbol{a}_n = \mathbf{Q}\boldsymbol{a}_{n-1} + \boldsymbol{D}. \tag{31}$$

3.3 Stability Prediction. The stability of the dynamic map equation and the system it describes is determined from the eigenvalues of the transition matrix $\mathbf{Q}=\mathbf{A}^{-1}\mathbf{B}$ [31–33,36,40,41]. If the magnitude of any eigenvalue is greater than one for a given spindle speed (Ω) and depth of cut (b), the milling process is considered unstable. Two distinct types of instability are illustrated by eigenvalue trajectories in the complex plane: (1) a flip

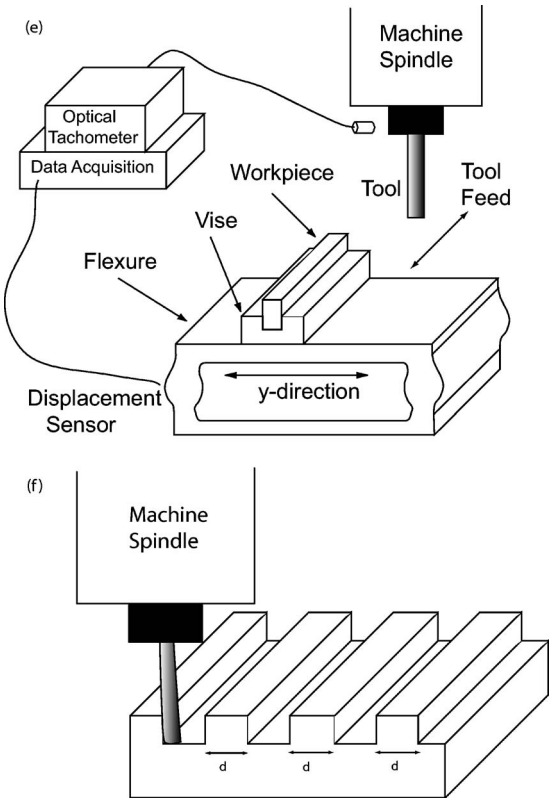

Fig. 4 Schematic diagram of surface location error experiments: (e) workpieces were mounted on a single degree of freedom flexure and up-milled in the compliant workpiece and rigid tool tests; and (f) down-milling was used in the compliant tool and rigid workpiece tests.

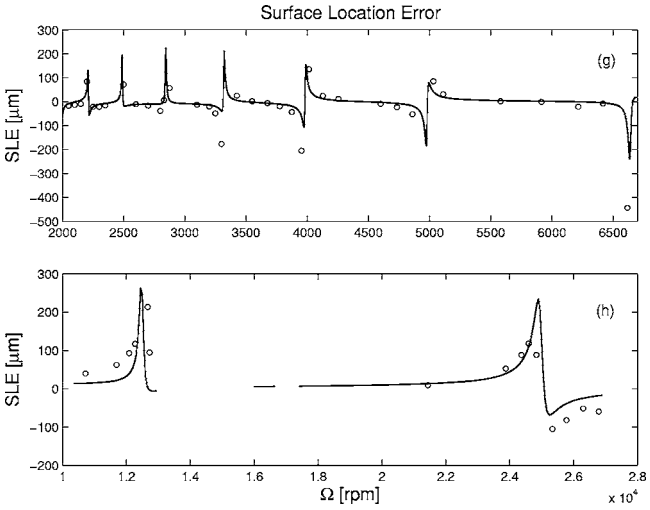

Fig. 5 Comparisons of TFEA fixed point predictions and measured surface location error (∘ indicates a measurement value): (g) Up-milling surface location error measurements for a single degree of freedom flexure obtained with an eddy current displacement transducer; and (h) Down-milling surface location error experimental results for the 19.05 (mm) tool of Table 1.

bifurcation or period-doubling phenomenon occurs when a negative real eigenvalue passes through the unit circle; and (2) a Hopf bifurcation occurs when a complex eigenvalue obtains a magnitude greater than one [31–33,36,41]. The stability predictions from a simple time marching scheme, as described in Ref. [1], have been compared to TFEA stability predictions in Fig. 2. Since the transition from stable to unstable cutting is not directly given with time marching, the variance of the 1/tooth passage displacements was applied [42]. Both numerical and analytical predictions show strong agreement.

3.4 Surface Location Error. The accurate placement of a surface is affected by imperfect spindle motions, thermal errors, controller errors, friction in the machine drives, machine geometric errors, and relative dynamic motions between the tool and workpiece [1,4,43]. This section presents a predictive method for the steady-state error due to tool or workpiece vibrations. In previous literature [4,6,28,33,43–45], this phenomena has been described as the "surface location error" from process dynamics.

The TFEA method discretizes the continuous system equations to form the dynamic map shown in Eq. (31). The coefficient vector $\boldsymbol{a}_n$ identifies the x- and y-displacements at the beginning and end of each element. Surface location error is given by the displacement coefficient that corresponds to when the cutting teeth produce the final surface. For a zero helix tool, this occurs at cutter entry for up-milling and cutter exit for down-milling.

Stable milling processes have periodic cutting forces and periodic solutions. The steady-state coefficients are found from the fixed points ($\boldsymbol{a}_n^*$) of the dynamic map:

$$\boldsymbol{a}_n = \boldsymbol{a}_{n-1} = \boldsymbol{a}_n^*. \tag{32}$$

Substitution of Eq. (32) into Eq. (31) gives the fixed point map solution or steady-state coefficient vector:

$$\boldsymbol{a}_n^* = (\mathbf{I} - \mathbf{Q})^{-1}\boldsymbol{D}. \tag{33}$$

Since $\boldsymbol{Q}$ and $\boldsymbol{D}$ can be computed exactly for each spindle speed and depth of cut, the fixed point displacement solution can be found and used to specify surface location error as a function of machining process parameters.

3.5 Time Series Reconstruction. The fixed point coefficient vector ($\boldsymbol{a}_n^*$) describes the tool-axis displacement and velocity at the beginning and end of each element. In some instances, such as in predicting the surface quality of a cutting process, it is desirable to

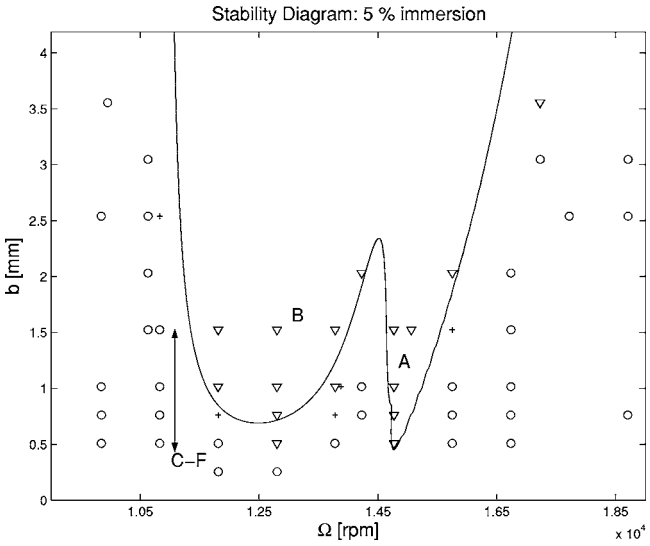

Fig. 6 Down-milling experimental results vs TFEA stability predictions for the 12.75 (mm) tool described in Table 1. The symbols in the above diagram are as follows: (a) ∘ is a clearly stable case; (b) ▽ is an unstable cutting test; and (c) + is a borderline unstable case (i.e., not clearly stable or unstable).

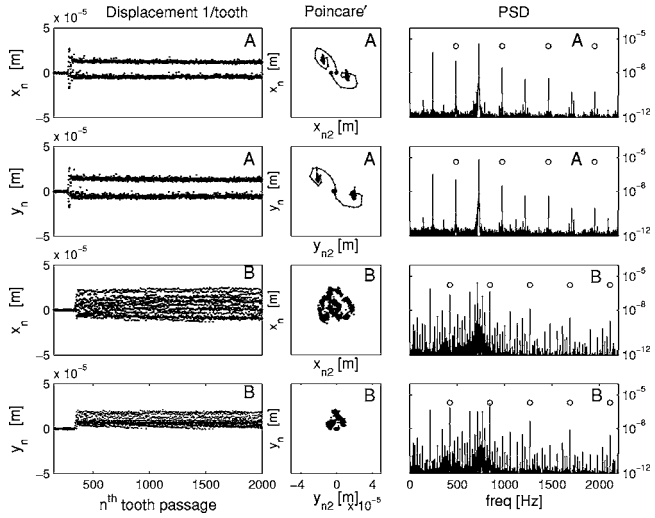

Fig. 7 Experimental down-milling measurement data for cases A and B of Fig. 6. Each row contains a 1/tooth passage displacement plot, a Poincaré section shown in delayed coordinates, and a Power Spectral Density (PSD) plot where ∘ marks the tooth passage frequency. Case A [Ω=14625 (rpm), b=1.0(mm)] is an example of an unstable period-doubling phenomenon or a flip bifurcation. Case B [Ω=12675 (rpm), b=1.5 (mm)] is an unstable Hopf bifurcation.

reconstruct the temporal field variables (i.e., displacement). This is performed by substituting the trial functions and fixed point displacement coefficients into Eq. (21). Two examples that compare a simulated time series to the TFEA reconstructed time series are shown in Fig. 3.

4 Experimental Verification

This section describes the results for three different experiments performed to verify analytical models. Stability predictions, for a compliant tool and rigid workpiece, are compared to experimental cutting test. Surface location error predictions are compared to the following experiments: (1) a flexible workpiece and rigid tool; and (2) a rigid workpiece and flexible tool. Cutting coefficients in the tangential and normal directions were determined during separate cutting tests on a Kistler Model 9255B rigid dynamometer [32,34]. The estimated cutting coefficient values for the aluminum (7050-T7451) material were $K_t=5.36\times10^8$ (N/m^2), $K_n=1.87\times10^8$ (N/m^2), $K_{te}=2.9\times10^3$ (N/m), and $K_{ne}=1.4\times10^3$ (N/m).

4.1 Surface Location Error Experiments. The first series of surface location error tests, developed to provide results for a compliant workpiece and rigid tool, were performed on Cincinatti Sabre 750 (commercial equipment is identified for completeness and does not imply endorsement by the authors) machining center using a single degree of freedom flexure (see Fig. 4). The compliant direction of the structure was oriented perpendicular to the tool feed. A single flute, 19.05 (mm) diameter, carbide end mill was used to up-mill both sides of aluminum (7050-T7451) test specimens at a radial immersion of 14%. Each test specimen, of length 100 (mm) and width 12.7 (mm), was machined at a different spindle speed while holding the feed and depth of cut at constant values of h=0.203 (mm/rev) and b=1.50 (mm) for all cutting tests. Flexure displacements were measured with an eddy current displacement transducer and a timing pulse from a laser tachometer. Surface location error was inferred from the flexure measurements and verified with measurements of the part surface [46]. Experimental results have been overlaid onto fixed point TFEA surface location error predictions in Fig. 5. The following are the flexure modal parameters estimated from impact testing (m_y)=0.692 (kg), (c_y)=7.216 (N s/m), $(k_y)=3.01\times10^6$ (N/m). Additionally, it is important to note the stiffness of the cutting tool was more than 20 times that of the flexure.

A second series of experiments, developed to provide results for a compliant tool and rigid workpiece, were performed on a 5-axis linear motor Ingersol machining center with a Fischer 40,000 (rpm), 40 (kW) spindle. The cutting tool was a two flute, 19.05 (mm) diameter, 106 (mm) overhang, carbide end mill. The test piece was first prepared by machining slots in an aluminum (7050-T7451) block (see Fig. 4). Finishing passes, performed at a cutting speed with minimal predicted error (Ω=18,500 (rpm), 5% immersion), were then used to size the island-shaped features to a final reference dimension of d=19.05 (mm).

Each side of the 250 (mm) long island was down-milled at a 5% radial immersion while keeping the feed and depth of cut constant [h=0.191 (mm/tooth), b=2.03 (mm)]. Every island was machined at a different spindle speed to illustrate the effect of changing process parameters on the final surface accuracy. The modal mass, damping, and stiffness parameters, shown in Table 1, were determined using the structural testing methods outlined in Refs. [47,48].

4.2 Stability Tests. Stability cutting tests were performed on a 5-axis linear motor Ingersol machining center with a Fischer 40,000 (rpm), 40 (kW) spindle. A 12.75 (mm) diameter, 106 (mm) overhang, carbide end mill was used during all stability tests (see modal parameters in Table 1). An aluminum (7050-T7451) block was down-milled at a 5% radial immersion and a feedrate of h=0.127 (mm/tooth); the spindle speed (Ω) and depth of cut (b) were changed for each cutting test to determine the onset of unstable vibrations. Since multiple cuts were performed on the same workpiece, a clean- up pass was performed prior to every recorded cut to create a reference surface.

Experimental stability results have been overlaid onto TFEA stability predictions (see Fig. 6). Tests were declared stable if the 1/tooth-sampled position approached a steady constant value [31,32,34,36,38]. Raw displacement measurements, measured 19 [mm] from the tool tip, were periodically sampled at the tooth passing frequency to create 1/tooth displacement samples and Poincaré sections shown in displacement vs delayed displacement coordinates; these plots are shown with the Power Spectral Density (PSD) of the continuously sampled displacement in Figs. 7 and 8 Unstable behavior, described as a flip bifurcation [3,32,33,38], is predicted when the dominant eigenvalue of the TFEA model is negative and real with a magnitude greater than one. Experimental evidence confirms this prediction where chatter is a subharmonic of order 2 for both the x- and y-axes (see case A of Fig. 7). Unstable behavior predicted by complex eigenvalues with a magnitude greater than one in the TFEA method corre-

Table 1 Compliant tool modal parameters

Diameter (mm)	**M** (kg)		**C** (N s/m)		**K** (N/m)	
19.05	0.061	0	3.86	0	1.67×10^6	0
	0	0.056	0	3.94	0	1.52×10^6
12.75	0.0436	0	4.268	0	9.14×10^5	0
	0	0.0478	0	4.355	0	1.00×10^6

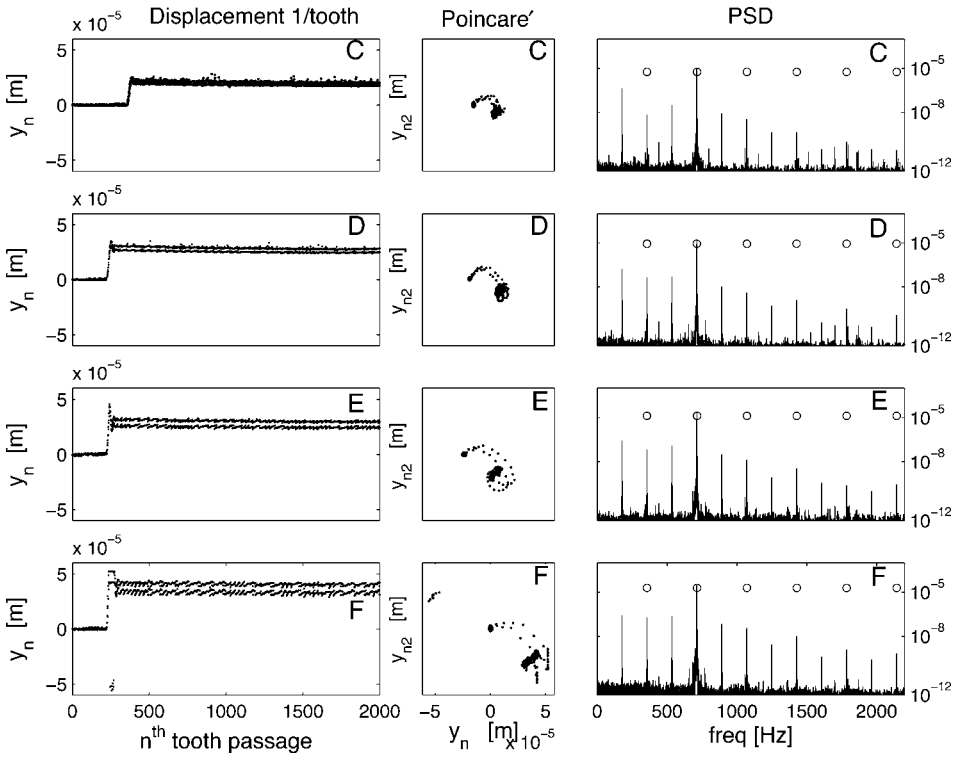

Fig. 8 Experimental down-milling measurement data for cases (C,D,E,F) of Fig. 6. Each row contains a *y*-axis 1/tooth displacement plot, a Poincaré section shown in delayed coordinates, and a Power Spectral Density (PSD) plot where ∘ marks the tooth passage frequency. Graphics show growth in the dynamic error between each tooth passage, associated with tool runout, for a fixed spindle speed and an increasing depth of cut C [Ω=10725 (rpm), *b*=0.5 (mm)], D [Ω=10725 (rpm), *b*=0.75 (mm)], E [Ω=10725 (rpm), *b*=1.0 (mm)], F [Ω =10725 (rpm), *b*=1.5 (mm)].

sponds to a Hopf bifurcation [25,31,32,40]. In such cases [49], chatter vibrations are unsynchronized with tooth passage as shown in case B of Fig. 7.

An interesting effect, not previously described in the literature [31–34,36,38], is shown by cases C–F of Fig. 8. While viewing the frequency content of the PSD would lead to the determination of stable behavior, a misleading stability assessment could be made from viewing the 1/tooth passage displacements plots and Poincaré sections (i.e., the displacement samples at each tooth passage do not approach the same equilibria solution). However, the Poincaré sections and 1/tooth displacement plots do show the tool oscillations exhibit periodicity as each of the individual cutting teeth make the surface. Cases C–F also show the error between consecutive tooth passages is scaled by the depth of cut. This behavior is a type of period-doubling, or subharmonic motion, that should not be mistaken for a predicted flip bifurcation because the PSD shows the dominant spectral content comes from the tooth passage frequency. The explanation for this phenomena is that synchronous error motions from runout will cause tool oscillation amplitudes to contain a 1/tooth perturbation. The results from Euler integration, which was used to verify the above hypothesis for cases C–F, are shown in Fig. 9.

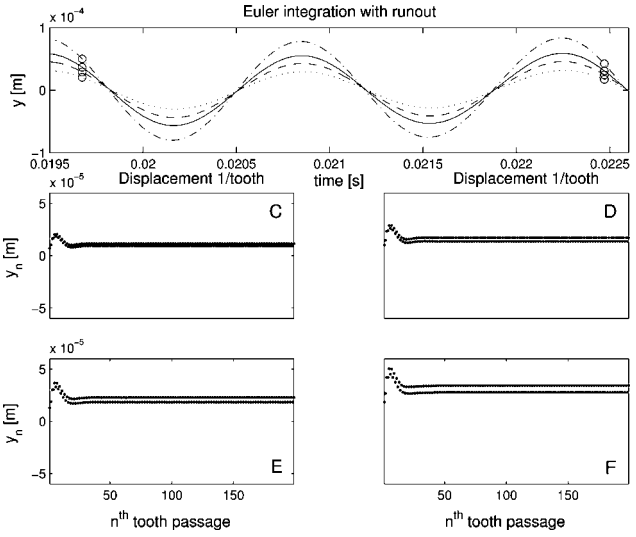

Fig. 9 Euler integration results for down-milling cases (C,D,E,F) of Fig. 6. The top graph shows two consecutive tooth passages, marked with ∘, and a continuous time trace with the following legend: (C, dotted line; D, dashed line; E, solid line; F, dashed-dotted line). The four bottom graphs are 1/tooth passage displacement samples showing the effect of runout on tool oscillations at the cutter exit.

5 Summary and Conclusions

Time finite element analysis is capable of providing simultaneous stability and surface location error predictions for milling. The TFEA method forms an approximate solution by dividing the time in the cut into a finite number of elements. The approximate solution is then matched with the exact solution for free vibration to obtain a discrete linear map. The formulated dynamic map is then used in three different ways: (1) stability prediction from the

magnitude of map characteristic multipliers; (2) prediction of steady-state surface location error from map fixed points; and (3) reconstruction of the stable cutting motion time series. This paper generalizes the TFEA solution procedure presented in previous work to model multiple modes in two orthogonal directions.

In this work, stability and surface location error predictions are compared to three different experimental cutting tests. Although relatively good agreement is obtained between predictions and experiment, the differences are considered to be related to: (1) the accuracy of system identification methods in identifying modal parameters; (2) the assumption that cutting forces linearly scale as a function of the uncut chip area; and (3) the assumption that measured cutting coefficients are unaffected by changes in spindle speed. In addition, the differences between predictions and the experiments for the rigid tool and compliant workpiece suffer from the assumption of an infinitely rigid tool. Stability tests show an interesting subharmonic motion, or period-doubling behavior, that was observed during experiments. This behavior, examined with a linear cutting force model, is not shown to destabilize tool oscillations. However, it does add a 1/tooth passage perturbation to the tool motions that may destabilize the system in the presence of structural or cutting force nonlinearities. The physical explanation for the observed behavior is shown to be the presence of runout in the cutter teeth.

Acknowledgment

Support from The Boeing Company, the National Science Foundation (CMS-0348288) and (DMII-0238019), and the ONR (2003 Young Investigator Program) is gratefully acknowledged.

References

[1] Tlusty, J., 2000, *Manufacturing Processes and Equipment*, 1st ed. Prentice-Hall, Upper Saddle River.
[2] Altintas, Y., 2001, "Analytical Prediction of Three Dimensional Chatter Stability in Milling," JSME Int. J., **44**, pp. 717–723.
[3] Davies, M. A., Pratt, J. R., Dutterer, B., and Burns, T. J., 2002, "Stability Prediction for Low Radial Immersion Milling," J. Manuf. Sci. Eng., **124**, pp. 217–225.
[4] Schmitz, T., and Ziegert, J., 1999, "Examination of Surface Location Error due to Phasing of Cutter Vibrations," Precis. Eng., **23**, pp. 51–62.
[5] Altintas, Y., 2000, *Manufacturing Automation*, 1st ed. Cambridge University Press, New York.
[6] Sutherland, J. W., and DeVor, R. E., 1986, "An Improved Method for Cutting Force and Surface Error Prediction in Flexible end Milling Systems," J. Eng. Ind., **108**, pp. 269–279.
[7] Tobias, S. A., 1965, *Machine Tool Vibration*, Blackie, London.
[8] Tlusty, J., Polacek, A., Danek, C., and Spacek, J., 1962, "Selbsterregte Schwingungen an Werkzeugmaschinen," VEB Verlag Technik, Berlin.
[9] Merritt, H., 1965, "Theory of Self-Excited Machine Tool Chatter," J. Eng. Ind., **87**, pp. 447–454.
[10] Pratt, J. R., and Nayfeh, A. H., 1999, "Design and Modeling for Chatter Control," Nonlinear Dyn., **19**, pp. 49–69.
[11] Koenisberger, F., and Tlusty, J., 1967, *Machine Tool Structures-Vol. 1: Stability Against Chatter*, Permagon, Oxford.
[12] Kegg, R. L., 1965, "Cutting Dynamics in Machine Tool Chatter," J. Eng. Ind., **87**, pp. 464–470.
[13] Shridar, R., Hohn, R. E., and Long, G. W., 1968, "A Stability Algorithm for the General Milling Process," J. Eng. Ind., **90**, p. 330.
[14] Hanna, N. H., and Tobias, S. A., 1974, "A Theory of Nonlinear Regenerative Chatter," J. Eng. Ind., **96**, pp. 247–255.
[15] Tlusty, J., and Ismail, F., 1983, "Special Aspects of Chatter in Milling," J. Vibr. Acoust., **105**, pp. 24–32.
[16] Grabec, I., 1988, "Chaotic Dynamics of the Cutting Process," Int. J. Mach. Tools Manuf., **28**, pp. 19–32.
[17] Stépán, G., 1989, *Retarded Dynamical Systems: Stability and Characteristic Functions*, John Wiley, New York.
[18] Minis, I., and Yanushevsky, R., 1993, "A New Theoretical Approach for Prediction of Machine Tool Chatter in Milling," J. Eng. Ind., **115**, pp. 1–8.
[19] Smith, S., and Tlusty, J., 1991, "An Overview of the Modeling and Simulation of the Milling Process," J. Eng. Ind., **113**, pp. 169–175.
[20] Altintas, Y., and Budak, E., 1995, "Analytical Prediction of Stability Lobes in Milling," CIRP Ann., **44**, pp. 357–362.
[21] Schultz, H., and Moriwaki, T., 1992, "High-Speed Machining," CIRP Ann., **41**, pp. 637–643.
[22] Nayfeh, A. H., Chin, C. M., and Pratt, J., 1997, "Applications of Perturbation Methods to Tool Chatter Dynamics," in *Dynamics and Chaos in Manufacturing Processes*, Wiley, New York.
[23] Balachandran, B., 2001, "Non-Linear Dynamics of Milling Process," Philos. Trans. R. Soc. London, Ser. A, **359**, pp. 793–819.
[24] Davies, M., and Balachandran, B., 2001, "Impact Dynamics in Milling of Thin-Walled Structures," Nonlinear Dyn., **22**, pp. 375–392.
[25] Stépán, G., and Kalmár-Nagy, T., 1997, "Nonlinear Regenerative Machine Tool Vibration," in *Proceedings of the 1997 ASME Design Engineering Technical Conference*, Sacramento, CA, No. DETC97/VIB-4021 (CD-ROM), p. n/a.
[26] Fofana, M. S., and Bukkapatnam, S. T., 2001, "A Nonlinear Model of Machining Dynamics," in *Proceedings of the 18th Biennial Conference of Mechanical Vibrations and Noise*, Pittsburgh, PA, No. DECT2001/VIB-21582, ASME.
[27] Zhao, M. X., and Baldachandran, B., 2001, "Dynamics and Stability of Milling Process," Int. J. Solids Struct., **38**, pp. 2233–2248.
[28] Montgomery, D., and Altintas, Y., 1991, "Mechanism of Cutting Force and Surface Generation in Dynamic Milling," J. Eng. Ind., **113**, pp. 160–168.
[29] Insperger, T., and Stépán, G., 2000, "Stability of High-Speed Milling," in *Proceedings of Symposium of Nonlinear Dynamics and Stochastic Mechanics*, No. AMD-241, Orlando, FL, pp. 119–123.
[30] Corpus, W. T., and Endres, W. J., 2000, "A High Order Solution for the Added Stability Lobes in Intermittent Machining," in *Proceeding of the Symposium on Machining Processes*, No. MED-11, pp. 871–878.
[31] Bayly, P. V., Halley, J. E., Mann, B. P., and Davies, M. A., 2001, "Stability of Interrupted Cutting by Temporal Finite Element Analysis," in *Proceedings of the 18th Biennial Conference on Mechanical Vibration and Noise*, Pittsburgh, PA, No. VIB-21581, ASME.
[32] Mann, B. P., Insperger, T., Bayly, P. V., and Stépán, G., 2003, "Stability of Up-Milling and Down-Milling, Part 2: Experimental Verification," Int. J. Mach. Tools Manuf., **43**, pp. 35–40.
[33] Mann, B. P., Bayly, P. V., Davies, M. A., and Halley, J. E., "Limit Cycles, Bifurcations, and Accuracy of the Milling Proces," J. Sound Vib., (in press).
[34] Halley, J. E., 1999, "Stability of Low Radial Immersion Milling," Master's thesis, Washington University, Saint Louis.
[35] Meirovitch, L., 1986, *Elements of Vibration Analysis*, 2nd ed., McGraw-Hill, New York.
[36] Bayly, P. V., Mann, B. P., Schmitz, T. L., Peters, D. A., Stépán, G., and Insperger, T., 2002, "Effects of Radial Immersion and Cutting Direction on Chatter Instability in End-Milling," in *Proceedings of the ASME Engineering Congress and Exposition*, New Orleans, LA, No. IMECE2002-34116, ASME.
[37] Peters, D. A., and Idzapanah, A. P., 1988, "Hp-Version Finite Elements for the Space-Time Domain," Comput. Mech., **3**, pp. 73–78.
[38] Bayly, P. V., Halley, J. E., Davies, M. A., and Pratt, J. R., 2001, "Stability Analysis of Interrupted Cutting with Finite Time in the Cut," in *Proceedings of ASME Design Engineering Technical Conference, Manufacturing in Engineering Division, Orlando, Florida*, No. MED-11, Orlando, FL, ASME, pp. 989–994.
[39] Jaluria, Y., 1986, *Computational Heat Transfer*, 1st ed., Hemisphere, Washington.
[40] Virgin, L. N., 2000, *Introduction to Experimental Nonlinear Dynamics*, Cambridge University Press, Cambridge.
[41] Insperger, T., Mann, B. P., Stépán, G., and Bayly, P. V., 2003, "Stability of Up-Milling and Down-Milling, Part 1: Alternative Analytical Methods," Int. J. Mach. Tools Manuf., **43**, pp. 25–34.
[42] Schmitz, T. L., 2003, "Chatter Recognition by a Statistical Evaluation of the Syncronously Sampled Audio Signal," J. Sound Vib., **262**, pp. 721–730.
[43] Stephenson, D. A., and Agapio, J. S., 1997, *Metal Cutting Theory and Practice*, 1st ed. Marcel Dekker, New York.
[44] Schmitz, T. L., Bayly, P. V., Soons, J. A., and Dutterer, B., 2001, "Prediction of Surface Location Error by Time Finite Element Analysis and Euler Integration," in *Proceedings of the 17th Annual ASPE Meeting, October 20–25*, American Society for Precision Engineering, pp. 132–137.
[45] Kline, W. A., Devor, R. E., and Shareef, I., 1982, "Prediction of Surface Accuracy in End Milling," J. Eng. Ind., **104**, pp. 272–278.
[46] Mann, B. P., Young, K. A., Schmitz, T. L., Bartow, M. J., and Bayly, P. V., 2003, "Machining Accuracy due to Tool or Workpiece Vibrations," in *Proceedings of ASME International Mechanical Engineering Congress and Exposition*, Washington, D.C., No. IMECE2003-41991, ASME.
[47] Pandit, S. M., 1991, *Modal and Spectrum Analysis: Data Dependent Systems in State Space*, 1st ed., Wiley, New York.
[48] Ewins, D. J., 1985, *Modal Testing: Theory and Practice*, Wiley, New York.
[49] Davies, M. A., Pratt, J. R., Dutterer, B., and Burns, T. J., 2000, "The Stability of Low Radial Immersion Machining," CIRP Ann., **49**, pp. 37–40.